Commun. Comput. Phys.
doi: 10.4208/cicp.OA-2017-0007

Vol. **22**, No. 3, pp. 863-888
September 2017

Equilibrium Configurations of Classical Polytropic Stars with a Multi-Parametric Differential Rotation Law: A Numerical Analysis

Federico Cipolletta[1,2], Christian Cherubini[3,4,*], Simonetta Filippi[3,4], Jorge A. Rueda[1,2,5] and Remo Ruffini[1,2,5]

[1] *Dipartimento di Fisica and ICRA, Sapienza Università di Roma, P.le Aldo Moro 5, I–00185 Rome, Italy.*
[2] *ICRANet, Piazza della Repubblica 10, I–65122 Pescara, Italy.*
[3] *Unit of Nonlinear Physics and Mathematical Modeling, University Campus Bio-Medico of Rome, Via A. del Portillo 21, I–00128 Rome, Italy.*
[4] *International Center for Relativistic Astrophysics-ICRA, University Campus Bio-Medico of Rome, Via A. del Portillo 21, I–00128 Rome, Italy.*
[5] *ICRANet-Rio, Centro Brasileiro de Pesquisas Físicas, Rua Dr. Xavier Sigaud 150, Rio de Janeiro, RJ, 22290–180, Brazil.*

Received 13 January 2017; Accepted (in revised version) 27 February 2017

Abstract. In this paper we analyze in detail the equilibrium configurations of classical polytropic stars with a multi-parametric differential rotation law of the literature using the standard numerical method introduced by Eriguchi and Mueller. Specifically we numerically investigate the parameters' space associated with the velocity field characterizing both equilibrium and non-equilibrium configurations for which the stability condition is violated or the mass-shedding criterion is verified.

PACS: 04.40.-b, 02.30.Jr, 02.60.-x

Key words: Free boundary problems, self-gravitating systems, numerical methods for partial differential equations.

1 Introduction

The problem of equilibrium of rotating self-gravitating systems, dating back to Newton's Principia Mathematica studies on the Earth's shape, still represents a very actual topic in

*Corresponding author. *Email addresses:* cipo87@gmail.com (F. Cipolletta), c.cherubini@unicampus.it (C. Cherubini), s.filippi@unicampus.it (F. Filippi), jorge.rueda@icra.it (J. A. Rueda), ruffini@icra.it (R. Ruffini)

 ©2017 Global-Science Press

https://doi.org/10.4208/cicp.OA-2017-0007 Published online by Cambridge University Press

the field of astrophysics. Its main target is to reconstruct the structure of rotating stars considered to be, in a first approximation, in hydrostatic equilibrium although more complicated hydrodynamical effects can be taken into account by using modern tools of numerical analysis. Historically the studies on spherical non rotating self-gravitating bodies (well summarized in the classical Chandrasekhar's monograph on stellar structure [1]) and on uniformly rotating ones in the case of incompressible fluids (deeply analysed too in the companion Chandrasekhar's monograph on ellipsoidal figures of equilibrium [2], as well as, for instance, in [4–12]) preceded the study of compressible uniformly rotating polytropic stars [3]. All of these studies were completed by a series of refined numerical integrations of the complicated field equations governing the problem, performed by the Japanese school, which specifically investigated the problem of self-gravitating fluid's shape bifurcations [13–20]. The next step then has been the inclusion of differential rotation laws in the treatment, for instance in [21, 22], where rotation profiles were considered admitting an exact integral relation leading to an analytical expression of the centrifugal potential term in the hydrostatic equilibrium equation. In the literature it is known that differential rotation plays an important role in modelling the rotating stars' structure, in particular for both initial and ending phases of the stars' life. Most of the aforementioned works dealt with barotropic stars, i.e. configurations in which isopycnic (constant density) and isobaric (constant pressure) surfaces coincide, although it has been recently stressed the importance to consider also more general situations, like the baroclinic one (in which isopycnic surfaces are inclined over isobaric ones) in order to obtain more realistic configurations [23]. We have to point out also that although many recent papers dealt with relativistic figures of equilibrium (see for instance e.g. [24] and references therein) in relation to the problem of modelling possible sources of gravitational waves, the initial step to investigate the effects of pure rotation is to consider the problem of classical figures of equilibrium first. In the present paper, we will analyse in detail i) a polytropic classical self-gravitating fluid, ii) with axial and equatorial symmetry and with iii) a multi-parametric differential rotation law, which was proposed in [25] without a systematic analysis of the possible configurations belonging to such a velocity profile. The main feature of this rotation profile is that, with respect to the study in [21], this one can be considered as a generalization because it does not admit an analytical expression for the integral for centrifugal potential term. In addition, the presence of different free-parameters allows a more detailed study of the way in which the star rotates. By using the general method given in [21] in order to perform an analysis of the free-parameters' space, we identify the presence of possible bifurcation points in the configurations' sequences. The article is organized as follows. In Section 2, the numerical method by Eriguchi and Mueller [21] is briefly reviewed, the multi-parametric differential rotation profile taken by [25] is discussed and an analysis of possible instabilities which may be reached is performed. In Section 3, we show results locating stable configurations within the free-parameters' space and focusing on how different values of parameters in the rotation law could lead to different shaped configurations. The correctness of results is checked and already known results of [21] are recovered. In Section 4 we summarize and

https://doi.org/10.4208/cicp.OA-2017-0007 Published online by Cambridge University Press

discuss the results obtained. Finally, details on the numerical implementation and on the definitions of physical quantities adopted in the analysis are given in Appendix A.

2 Theoretical framework

2.1 The problem of equilibrium

In this section we review the general method for analyzing rotating and self-gravitating fluids as presented in [21]. In this method the attention is focused on a configuration of rotating and self-gravitating gas for which the equation of hydrostationary equilibrium, in its differential form, reads

$$-(\vec{v}\cdot\vec{\nabla})\vec{v}=\frac{\vec{\nabla}P}{\rho}+\vec{\nabla}\Phi_g, \tag{2.1}$$

being $\vec{v}$, ρ, P and Φ_g respectively the fluid's velocity, density, pressure and gravitational potential. The latter quantity must satisfy the Poisson's equation, which for a general configuration reads

$$\Delta\Phi_g=\begin{cases} 4\pi G\rho, & \text{inside,} \\ 0, & \text{outside,} \end{cases} \tag{2.2}$$

being G the constant of gravitation. Note that left-hand side of Eq. (2.1) can be written as

$$-(\vec{v}\cdot\vec{\nabla})\vec{v}=-\frac{1}{2}\vec{\nabla}(\vec{v}\cdot\vec{v})-(\vec{\nabla}\times\vec{v})\times\vec{v}, \tag{2.3}$$

so that using Eq. (2.1) we get

$$\frac{\vec{\nabla}P}{\rho}+(\vec{\nabla}\times\vec{v})\times\vec{v}=-\left(\vec{\nabla}\Phi_g+\frac{1}{2}\vec{\nabla}(\vec{v}\cdot\vec{v})\right), \tag{2.4}$$

and as the right-hand side has null curl, one obtains the following integrability condition for Eq. (2.1)

$$\vec{\nabla}\times\left\{\frac{\vec{\nabla}P}{\rho}+(\vec{\nabla}\times\vec{v})\times\vec{v}\right\}=0. \tag{2.5}$$

Writing explicitly the fluid's velocity of a rotating gas in hydrostationary equilibrium in cylindrical coordinates (ϖ,z,ϕ) as

$$\vec{v}=\varpi\Omega(\varpi,z)\hat{e}_\phi, \tag{2.6}$$

one obtains that Eqs. (2.1) and (2.5) are respectively equivalent to

$$\frac{\vec{\nabla}P}{\rho}=-\nabla\Phi_g+\varpi\Omega^2(\varpi,z)\hat{e}_\varpi, \tag{2.7}$$

$$2\varpi\Omega(\varpi,z)\frac{\partial\Omega(\varpi,z)}{\partial z}\hat{e}_\phi=\vec{\nabla}\frac{1}{\rho}\times\vec{\nabla}P. \tag{2.8}$$

https://doi.org/10.4208/cicp.OA-2017-0007 Published online by Cambridge University Press

From Eq. (2.8), by assuming a barotropic Equation of State (EOS), $P=P(\rho)$, we get

$$\frac{\partial\Omega}{\partial z}=0, \tag{2.9}$$

which is a well known sufficient condition (see [26]) for isopycnic (constant density) and isobaric (constant pressure) surfaces to be coincident. In addition, we also obtain that the centrifugal term in Eq. (2.7) comes out from a potential which can be defined as

$$\Phi_c=-\int_0^{\varpi}\varpi'\Omega^2(\varpi')d\varpi'. \tag{2.10}$$

One can in principle investigate Eqs. (2.2) and (2.7) in their differential form, but this gives rise to problems in treating the boundary conditions to impose, which are the finiteness of Φ_g and P at the center of the star, the vanishing of Φ_g at infinity and the definition of the surface where P vanishes. On the other hand, by treating the integral form of these equations, one can incorporate the boundary condition in an easier way. To do so, we have to note that Φ_g at a point $\vec{x}$, due to the presence of mass in the volume V, can be written as (see e.g. [27])

$$\Phi_g(\vec{x})=-G\int_V\frac{\rho(\vec{x}')}{|\vec{x}-\vec{x}'|}dV', \tag{2.11}$$

which using spherical coordinates (r,θ,ϕ) together with axial and equatorial symmetries, is equal to

$$\begin{aligned}\Phi_g(r,\theta)=&-4\pi G\int_0^{\frac{\pi}{2}}\sin(\theta')d\theta'\int_0^{r_{\rm surf}(\theta)}r'^2dr'\\&\cdot\sum_{n=0}^{\infty}f_{2n}(r,r')P_{2n}(\cos(\theta))P_{2n}(\cos(\theta'))\rho(r',\theta').\end{aligned} \tag{2.12}$$

Here we indicate with $P_{2n}(\cos(\theta))$ the Legendre's polynomial of order $2n$ computed in $\cos(\theta)$ and f_{2n} are the Green's functions (of even order), defined by

$$f_{2n}(r,r')=\begin{cases}\frac{r'^{2n}}{r^{2n+1}} & \text{for } r\geq r',\\ \frac{r^{2n}}{r'^{2n+1}} & \text{for } r<r'.\end{cases} \tag{2.13}$$

It is possible now to have Eq. (2.1) in its integral form, which can be written as

$$\int\frac{1}{\rho}dP+\Phi_g+\Phi_c=C\ (\text{const.})\ . \tag{2.14}$$

The system to be solved is defined via Eq. (2.14) coupled to Eq. (2.12). But one still has to insert the EOS and the boundary conditions to define the surface (a free boundary problem) of the figure of equilibrium, namely

$$\rho(r_{\rm surf})=0 \tag{2.15}$$

https://doi.org/10.4208/cicp.OA-2017-0007 Published online by Cambridge University Press

and a rotation law, that is a relation to express Ω as a function of the adopted coordinates, which will be used in the centrifugal potential term, Φ_c. The choice of the EOS relation is one the most delicate points in approaching the problem of equilibrium of rotating gases from the physical point of view. In fact, different EOSs can result in very different configurations of equilibrium of rotating stars. For the sake of simplicity we suppose that the gas we are modelling is perfect, in the sense that it is composed of non-interacting particles (i.e. the effects of interacting particles is negligible, thus we can neglect viscosity implicated by energy dissipation during motion due to the interaction between particles) and it is non-degenerate (see e.g. [27]). An EOS which in a first approximation is able to model this kind of physical properties is the polytropic one

$$P = K\rho^{1+\frac{1}{n}}, \tag{2.16}$$

where K is the polytropic constant and n is the polytropic index. At this point, the only missing ingredient to numerically solve the system of equations (which we report in Appendix A) is a rotation profile.

2.2 Multi-parametric differential rotation law

When integrating hydrostationary equilibrium equation together with Poisson's equation on a discretized numerical grid (see Appendix A for details) one should also supply a rotation law, i.e. a relation to express the angular velocity on each grid-point as a function of the spatial variables. In particular, actually we are interested in the study of the axisymmetric case, in which equatorial symmetry is also prescribed, thus a natural choice of coordinates' set will be the spherical one (r,θ,ϕ). In literature many cases have already been studied, taking into account both uniform rotation, i.e. $\Omega = \text{const.}$ (see e.g. [3]), and differential rotation, i.e. $\Omega = \Omega(\varpi)$, being $\varpi = r\sin(\theta)$ the cylindrical radius (see e.g. [22] and [21]). More precisely, in papers dealing with differential rotation, a single-free-parameter differential rotation law is chosen, i.e. where $\Omega(\varpi)$ depends also on one single free parameter which allows to control how much differential is the rotation, in the sense that for a defined value the uniformly rotating case is recovered. We consider here a differential rotation law of the following kind (see Ref. [25]):

$$\Omega(\varpi) = \Omega_0 \frac{e^{-B\varpi^2}}{1+\left(\frac{\varpi}{A}\right)^2}, \tag{2.17}$$

being Ω_0 the central angular velocity and A and B parameters which control the rotation law and that in a limiting case can reproduce uniform rotation. It is worth noting that the if $A \to \infty$, the rotation law tends to the one of [22], while if $B = 0$, it is the so-called j-const. rotation law of [21]. Although it may seem that Ω_0, A and B are all free-parameters, the reader will see that Ω_0 is treated as an unknown by the method adopted, thus the actual free-parameters' number is two as the value of Ω_0 is obtained from the choice of the axis

https://doi.org/10.4208/cicp.OA-2017-0007 Published online by Cambridge University Press

ratio. We then require $A,B\geq 0$. It is useful to introduce dimensionless variables within the method, adopting the following relation:

$$F=k_F\tilde{F}, \tag{2.18}$$

where F is the physical quantity in real dimension, k_F is the constant for non-dimensionalization and $\tilde{F}$ is the quantity in dimensionless form. In particular, as in [21] we adopt non-dimensional constants as reported in Table 1, where n is the polytropic index, K is the polytropic constant and G is the gravitational constant. Looking at Eq. (2.17) is evident that parameters A and B have dimensions of length and length^{-2} respectively, thus it is also useful to impose

$$A=ar_{\rm s}, \tag{2.19}$$

$$B=\frac{b}{{r_{\rm eq}}^2}, \tag{2.20}$$

with $r_{\rm s}$ being the radius of the spherical configuration and $r_{\rm eq}$ the equatorial spherical coordinate radius, just like in [21] (for parameter A) and [22] (for parameter B). The main problem in choosing differential rotation given by Eq. (2.17), is that the integral to compute the centrifugal potential term in the hydrostationary equilibrium equation (see Section 2) cannot be performed analytically. For this reason we have decided to

Table 1: Constants adopted to obtain dimensionless quantities from Eq. (2.18).

F	k_F	$\tilde{F}$	Physical Meaning
ρ	ρ_c	σ^n	Density
P	$K\rho_c^{1+\frac{1}{n}}$	σ^{n+1}	Pressure
Ω^2	$[4\pi G\rho_c]$	ν	Squared Angular Velocity
Φ_g	$K(n+1)\rho_c^{\frac{1}{n}}$	Ψ	Gravitational Potential
r	$\left[\frac{K(n+1)}{4\pi G}\rho_c^{\frac{1}{n}-1}\right]^{\frac{1}{2}}$	ξ	Spherical Radius
M	$4\pi\left[\frac{K(n+1)}{4\pi G}\right]^{\frac{3}{2}}\rho_c^{\frac{3-n}{2n}}$	$\tilde{M}$	Mass
J	$\frac{[K(n+1)]^{\frac{5}{2}}}{4\pi G^2}\rho_c^{\frac{5-2n}{2n}}$	j	Angular Momentum
I_Ω	$\frac{[K(n+1)]^{\frac{5}{2}}}{[4\pi]^{\frac{3}{2}}G^{\frac{5}{2}}}\rho_c^{\frac{5-3n}{2n}}$	$\tilde{I}$	Moment of Intertia
T	$\frac{[K(n+1)]^{\frac{5}{2}}}{[4\pi]^{\frac{1}{2}}G^{\frac{3}{2}}}\rho_c^{\frac{5-n}{2n}}$	$\tilde{T}$	Kinetic Energy
W	$\frac{[K(n+1)]^{\frac{5}{2}}}{[4\pi]^{\frac{1}{2}}G^{\frac{3}{2}}}\rho_c^{\frac{5-n}{2n}}$	$\tilde{W}$	Gravitational Potential Energy
U	$\frac{[K(n+1)]^{\frac{5}{2}}}{[4\pi]^{\frac{1}{2}}G^{\frac{3}{2}}}\rho_c^{\frac{5-n}{2n}}$	$\tilde{U}$	Thermal Energy

https://doi.org/10.4208/cicp.OA-2017-0007 Published online by Cambridge University Press

perform a numerical integration (via trapezoidal method) on an artificial numerical grid for each axis distance from the particular grid-point in which to compute the value of centrifugal potential, considering a very large set of $N_{\rm cyl}$ points (namely $N_{\rm cyl}=1000$ for each grid-point and $N_{\rm cyl}=10000$ to find the integration constant). With such numerical grid in the cylindrical radial coordinate, the aforementioned numerical integration for the centrifugal potential is able to properly reproduce already known results [21] (see Section 4). This allows us to study in a general numerical way every kind of differential rotation law, without requiring an analytical form for centrifugal potential.

2.3 Stability

As already pointed out in [22], an important condition which the chosen rotation law should satisfy is the stability condition against axisymmetric perturbation, provided by the Solberg-Høiland criterion,

$$\frac{d\left[\varpi^2\Omega(\varpi)\right]}{d\varpi}>0, \tag{2.21}$$

which states that the angular momentum per unit mass $\varpi^2\Omega$ must increase outwards (c.f. [22], [26] and [27]), i. e. going from the pole to the equator (for a complete derivation of this criterion we refer to [28]). Thus, when choosing a rotation law, one must always verify that Eq. (2.21) is satisfied in order to guarantee stability. Using Eq. (2.17) in Eq. (2.21), it is easy to check that this condition is equivalent to

$$B\varpi^2A^2+B\varpi^4-A^2<0, \tag{2.22}$$

which, using definitions given in Eqs. (2.19), (2.20) and in Table 1 for r and simplifying for a factor ${K_r}^2$, in dimensionless form reads as:

$$\frac{b}{{\xi_{\rm eq}}^2}\widetilde{\varpi}^2a^2{\xi_{\rm s}}^2+\frac{b}{{\xi_{\rm eq}}^2}\widetilde{\varpi}^4-a^2{\xi_{\rm s}}^2<0, \tag{2.23}$$

where $\widetilde{\varpi}=\xi\sin(\theta)$ is the dimensionless cylindrical radius, $\xi_{\rm eq}$ is the dimensionless spherical equatorial radius of the configuration and $\xi_{\rm s}$ is the dimensionless radius of the initial spherical configuration. It is now evident that the stability condition may be violated for particular choices of the two free-parameters. It could be interesting to have a sample of what violation of criterion of Eq. (2.21) would imply. Anticipating some results, in Fig. 1 the angular momentum per unit mass distribution along the distance from rotation axis direction is plotted for three configurations, obtained with same differential rotation exponential parameter $b=0.128$ and axis ratio $\frac{r_{\rm eq}}{r_{\rm pol}}=1.05$ but with different choices of parameter a (namely 0.02,1.12,2.00). It can be noted that for sequences represented by dashed and dash-dotted curves (respectively with $a=1.12$ and $a=2.00$) the condition of Eq. (2.21) is obviously satisfied, leading to stable configurations and allowing the entire sequence to be constructed (as the reader will see in figures of next section), while for sequence represented by solid the curve, obtained with $a=0.02$, the angular momentum

https://doi.org/10.4208/cicp.OA-2017-0007 Published online by Cambridge University Press

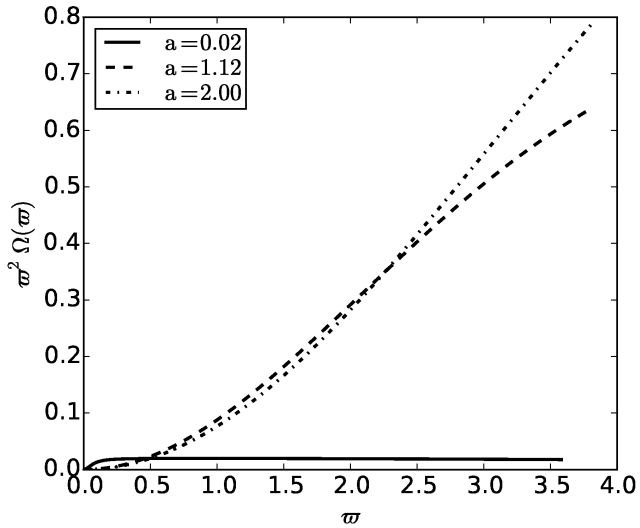


Figure 1: Angular momentum per unit mass distribution along distance from rotation axis for three sample sequences obtained with same choice of parameter $b=0.128$ and axis ratio $\frac{r_{\rm eq}}{r_{\rm pol}}=1.05$, but different choices of parameter $a=0.02,\ 1.12,\ 2.00$.

per unit mass distribution is slowly decreasing. The stability condition given by Eq. (2.21) is not the only one to be controlled. In fact, another physical limit for the rotation which is worth to take into account is the mass-shedding limit, namely the point in which the rotation becomes too fast to allow stability. As already presented in [3] or [26] the aforementioned limit for equilibrium configurations in the axisymmetric case occurs when the effective gravity of the surface at the equator becomes zero, which means that the gravitational force is perfectly balanced by the centrifugal one (and vice-versa). Actually, if the angular velocity would increase further after this condition is reached, a portion of the total mass should begin to shed from the star, because the centrifugal force would become greater than the gravitational one (the so-called "mass-shedding"). Using a polytropic EOS and the constants for dimensionless form given by Table 1, one gets the following criterion for dimensionless effective gravity

$$\tilde{g}_{\rm eq\ eff}=\frac{\partial\sigma}{\partial\tilde{\xi}}\left(\xi_{\rm surf\ eq},\frac{\pi}{2}\right)\leq 0, \tag{2.24}$$

necessary to avoid mass-shedding.

3 Results

3.1 Differentially rotating polytropes

In the following analyses, we have specifically adopted for the polytropic relation of Eq. (2.16) the value $n=1.5$. Adopting a multi-parametric differential rotation law, such

https://doi.org/10.4208/cicp.OA-2017-0007 Published online by Cambridge University Press

the one given in Eq. (2.17), it is possible to have a very detailed control on the way the star rotates. It is interesting to understand the different figures of equilibrium which could result from different choices of these control parameters. Summarizing, to perform such an analysis, one can use the method given in [21] to build several equilibrium sequences, each obtained by a fixed change in the axis ratio from one configuration to another (see Section 2), taking into account the Solberg-Høiland criterion in Eq. (2.21) and the mass-shedding condition given in Eq. (2.24). Thus, we decided to fix initial extrema for parameters value, namely $a_{\min}$, $a_{\max}$, $b_{\min}$ and $b_{\max}$ and to compute respectively N_a and N_b linearly equally spaced parameter's values between these extremes. Explicitly, the parameters value are given by the following equation:

$$p_k = p_{\min} + \left((p_{\max} - p_{\min}) \times \frac{(k-1)}{(N_p - 1)} \right) \quad \text{for } k = 1, \cdots, N_p, \tag{3.1}$$

where with letter p the parameter's name is intended, namely a or b. After having fixed the set of values for free-parameters, several sequences can be computed starting from the spherical configuration until some kind of instability is reached. However we notice that it is possible that none of the two instability condition could be reached, thus we decided to stop the computations when 101 configurations have been built (this in order to limit the computation time). Precisely, the maximum axis ratio of equilibrium configurations which is reached in this way is $(1.05)^{101} \sim 138.07$.

In Fig. 2 the kind of instability reached (after the entire sequence is computed) for each choice of the two rotational parameters is represented, with color convention given in the

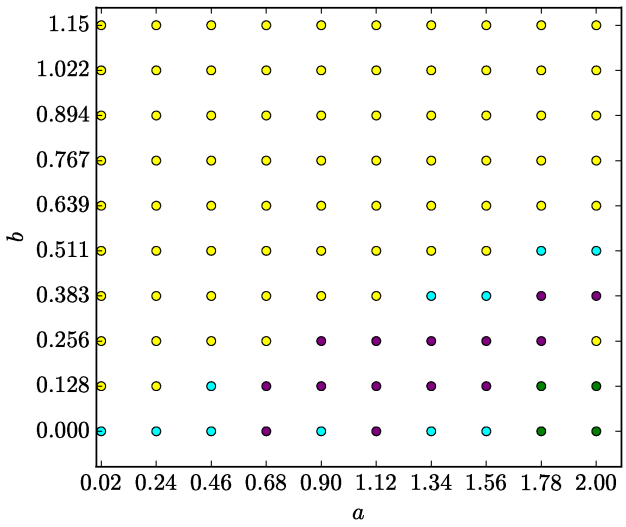


Figure 2: Resulting equilibrium configurations for different choices of rotational parameters b and a of Eq. (2.17), obtained with 15-angular times 40-radial points in the numerical grid. Colour convention is: green is for mass-shedding criterion violation, yellow is for Solberg-Høiland criterion violation, blue is for concave hamburger configurations, which after 101 configurations did not violate any stability criterion and purple is for concave hamburger configuration which reach mass-shedding at equator.

https://doi.org/10.4208/cicp.OA-2017-0007 Published online by Cambridge University Press

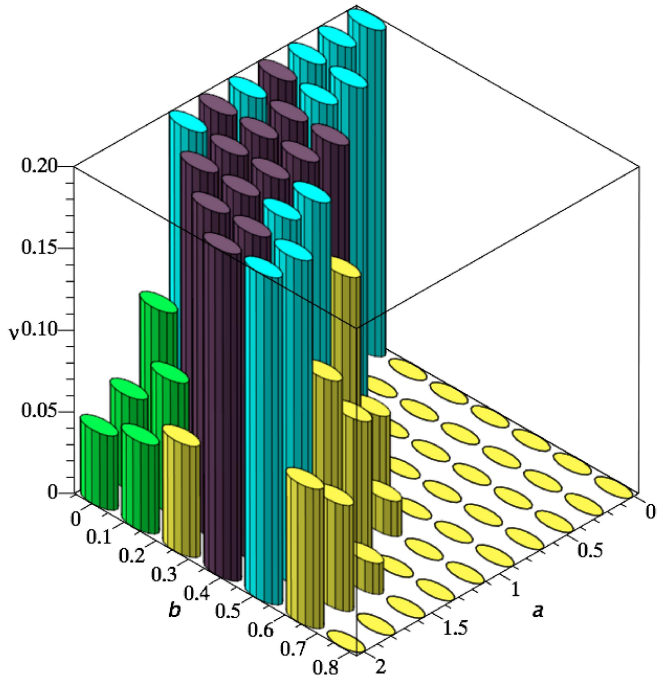


Figure 3: Same as Fig. 2, but with a 8×22 points numerical grid, where in vertical axes is indicated the maximum value of dimensionless central angular velocity of the last stable configuration for each sequence of configurations computed (squeezing for visual purposes).

caption. Here, computations where performed with a 15×40 points numerical grid. From this figure, it is clear that, depending on the choice of rotational parameters, different kinds of configurations can result. It is interesting to study the parameters' space in three dimensions, e.g. taking into account the maximum value of central dimensionless angular velocity reached in each sequence.

In Fig. 3 a three-dimensional plot of the aforementioned kind is presented. It has been obtained considering in x-y plane the same as Fig. 2 and in the vertical axes the maximum dimensionless central angular velocity reached by configurations in each sequence of configurations just before the different kinds of instability occur, but considering a 8×22 points numerical grid. In particular, it is worth noting that the value of central angular velocity goes well beyond the value of 0.2 for each sequence in which a concave hamburger structure appears (this nomenclature follows [17]). This is due to the fact that effective gravity slightly increases along these sequences, although in some cases mass-shedding occurs before the limit of 101 configurations is reached. In addition, some evident differences in color of points of Fig. 2 and Fig. 3 must be underlined manifesting the strong grid-dependence of the model implemented. In Figs. 4, 5, 6 and 7 density distributions of some configurations are plotted, revealing also the shape of configuration. In particular, Fig. 4 is obtained through the solution of Lane-Emden equation (see Appendix A) for the construction of the spherical configuration. From this configuration,

https://doi.org/10.4208/cicp.OA-2017-0007 Published online by Cambridge University Press

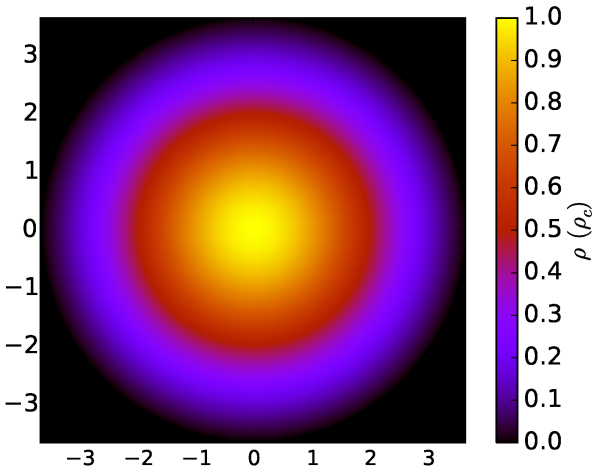


Figure 4: Density distribution for spherical configuration obtained via solution of Lane-Emden equation (see Appendix A).

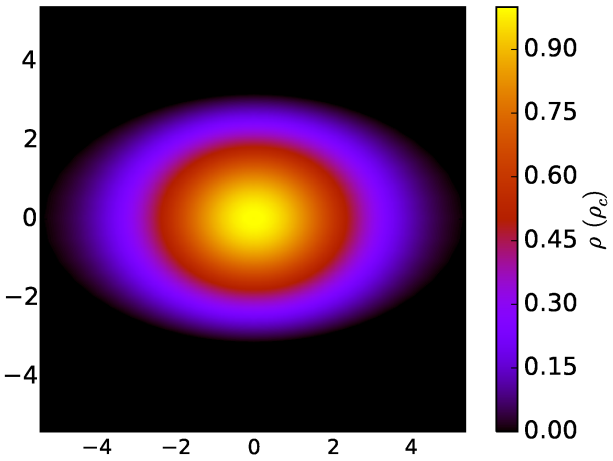


Figure 5: Density distribution for an oblate configuration, obtained fixing b=0.0 and a=2.0 in Eqs. (2.17), (2.19) and (2.20). The axis ratio value here is $\frac{r_{\rm eq}}{r_{\rm pol}}=1.71$, thus the oblateness is evident. This kind of configuration will undergo to mass-shedding instability, according to Fig. 2.

all the other configurations are obtained by increasing the axis ratio with the method described in Section 2, fixing several values for differential rotation parameters. In Fig. 5, fixing $b=0$ and $a=2.0$ in Eqs. (2.19) and (2.20) and increasing the axis ratio value up to $\frac{r_{\rm eq}}{r_{\rm pol}}=1.71$, produces an evident oblate structure, in which the equatorial centrifugal force will increase until a mass-shedding instability is reached (see Fig. 2). Finally, Figs. 6 and 7 belong to the same sequence of configurations, obtained fixing $b=0.128$ and $a=0.46$ in Eqs. (2.19) and (2.20), respectively with $\frac{r_{\rm eq}}{r_{\rm pol}}=1.22$ and 7.04. In these two figures the forma-

https://doi.org/10.4208/cicp.OA-2017-0007 Published online by Cambridge University Press

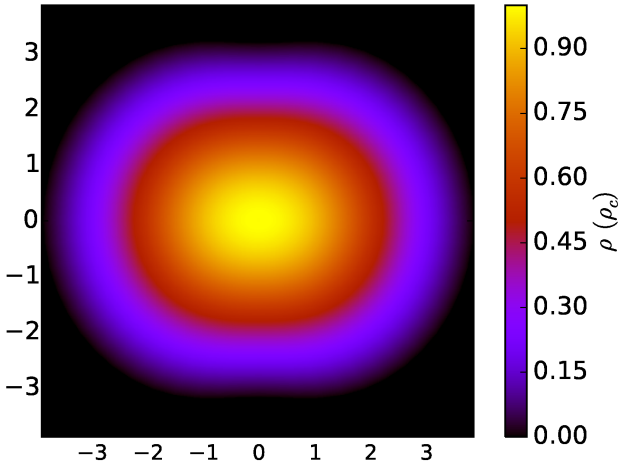


Figure 6: Density distribution for a configuration which is starting to be a concave hamburger one, obtained fixing $b=0.128$ and $a=0.46$ in Eqs. (2.17), (2.19) and (2.20). The axis ratio value here is $\frac{r_{\rm eq}}{r_{\rm pol}}=1.22$ and although it is nearly spherical an accurate observation shows that the differential rotation parameters' value begin to create a oblate hamburger structure.

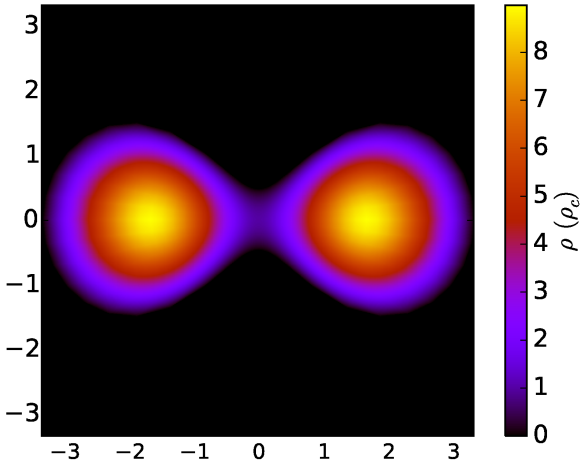


Figure 7: Same as Fig. 6, but with axis ratio value here fixed as $\frac{r_{\rm eq}}{r_{\rm pol}}=7.04$.

tion of a ring-like structure is evident: as the axis ratio increases, mass density maximum transfers from the center of configuration to a certain grid point and this process, with further increasing in axis ratio, would produce a torus (although in present calculation this result can not be seen, as the method is not appropriate for the study of ring-like structures, see [21] for details; in particular, the present method does not allow to see the hole formation leading to a toroidal configuration).

https://doi.org/10.4208/cicp.OA-2017-0007 Published online by Cambridge University Press

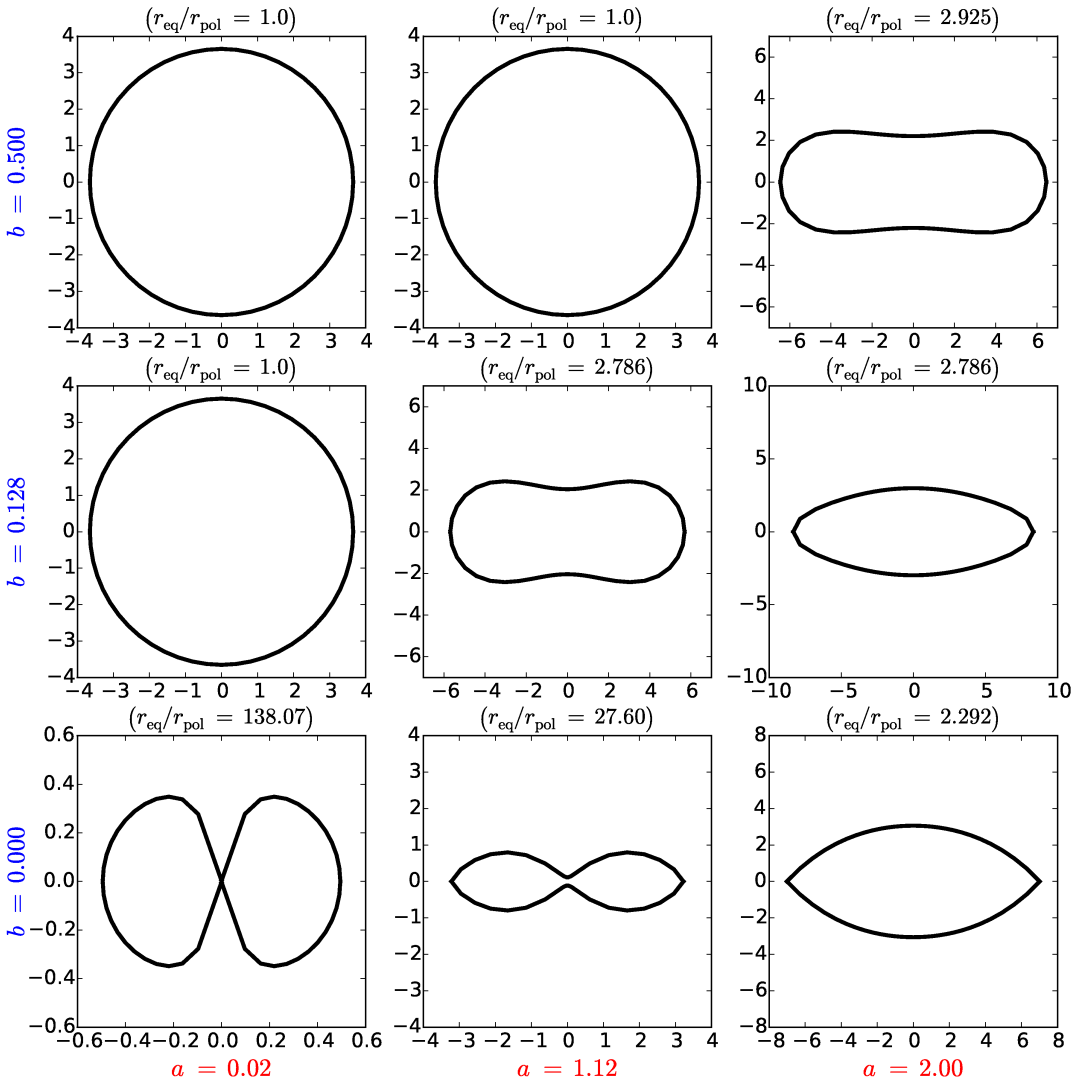


Figure 8: Sample of configurations surfaces for different choices of parameters of differential rotation. Figures show the last stable configurations just before computation is stopped because of aforementioned conditions (namely mass-shedding, violation of Solberg-Høiland criterion or error in N-R method's implementation). For each row and column of figures, values of parameters a and b of Eqs. (2.19) and (2.20) are indicated respectively with red and blue colors. Cusps are an artifact due to the absence of the graphical interpolation between two grid points.

In Fig. 8 we show some samples of possible figures of equilibrium which can be obtained using the differential rotation law of Eqs. (2.17), (2.19) and (2.20), with different choices of free parameters a and b. In particular, each plot corresponds to the last stable configuration which our code produced just before the computation has been stopped due to aforementioned possible reasons (namely mass-shedding, violation of stability criterion, exceeding in the number of configurations). The axis ratio r_{eq}/r_{pol} of each con-

https://doi.org/10.4208/cicp.OA-2017-0007 Published online by Cambridge University Press

figuration is reported in parentheses above each plot. A spherical figure means that the particular choice of rotational parameter leads immediately to some kind of instability (the reader should refer specifically to Fig. 2). Before concluding this section, an important consideration must be done. Our code adopts the Newton-Raphson (N-R) method as discussed in Ref. [29] in order to compute the solution of a set of non-linear equations. The code uses the LU decomposition method in order to invert the Jacobian matrix but we found in some cases instabilities. In fact, the Newton-Raphson method implemented could lead to local minima of the system, instead to an absolute one. For this reason and because of the strong grid-dependence of Eriguchi and Mueller method, in some cases, the computation could be interrupted for some particular choices of rotational parameters before one of the stopping conditions occurs. How can be possible to recover these missing result? In these cases the grid-dependence study helps us. In fact, one could perform some cross-checks between results obtained using several grids and this guarantees the accuracy of results presented. In particular, for results presented in this section, we compared results obtained with 8×22 and 15×40 grids. We also report in Tables 2-4, the physically relevant values of some of the sequences computed, exemplifying the different configurations of equilibrium obtained. It is worth noting that, although usually convergence may be recovered changing the initial guess, this is not possible for the present situation, because the computation is always starting from the spherically symmetric configuration, obtained by the solution of Eq. (A.9). We also tried to reduce the step of axis ratio from one configuration to another (e.g. 1.01), but neither this could give any benefit to the convergence.

Table 2: Results of our numerical computations for an almost uniformly rotating sequence of equilibrium configurations obtained fixing $b=0$ and $a=2.0$. This sequence will end in mass-shedding.

$\frac{\zeta_{\rm eq}}{\zeta_{\rm pol}}$	j^2	$\frac{\widetilde{T}}{\lvert\widetilde{W}\rvert}$	$\frac{\widetilde{U}}{\lvert\widetilde{W}\rvert}$	$\widetilde{M}$	V.T.
1.000	0.000000	0.000000	0.500	2.710	9.55e−4
1.158	0.972e−3	0.2861e−1	0.472	2.994	4.87e−4
1.276	0.165e−2	0.4607e−1	0.454	3.156	4.24e−4
1.407	0.234e−2	0.6242e−1	0.438	3.323	3.93e−4
1.551	0.304e−2	0.7720e−1	0.423	3.488	3.71e−4
1.710	0.369e−2	0.9003e−1	0.410	3.643	3.59e−4
1.886	0.425e−2	0.1002000	0.400	3.774	3.48e−4
2.078	0.465e−2	0.1069000	0.393	3.867	3.23e−4
2.292	0.487e−2	0.1102000	0.390	3.934	3.28e−4

3.2 Numerical tests

To test our results with ones from literature, we will refer to tables presented in [21], for the so-called *j-const* rotation law, for choices of parameter $A=2.0r_{\rm s}$, $0.2r_{\rm s}$ and $0.02r_{\rm s}$

https://doi.org/10.4208/cicp.OA-2017-0007 Published online by Cambridge University Press

Table 3: Results of our numerical computations for an almost uniformly rotating sequence of equilibrium configurations obtained fixing $b=0.0$ and $a=1.12$. This sequence will end in mass-shedding although it will also tend to have a concave hamburger structure.

$\frac{\tilde{\zeta}_{eq}}{\tilde{\zeta}_{pol}}$	j^2	$\frac{T}{\|W\|}$	$\frac{U}{\|W\|}$	$\widetilde{M}$	V.T.
1.000	0.000000	0.000000	0.500	2.710	9.55e−4
1.477	0.307e−2	0.8168e−1	0.419	3.565	4.23e−4
2.407	0.853e−2	0.1873000	0.313	6.146	5.43e−4
3.920	0.133e−1	0.2583000	0.242	17.172	6.54e−4
6.385	0.166e−1	0.2763000	0.224	47.965	9.09e−4
10.401	0.187e−1	0.2867000	0.214	114.025	7.76e−4
16.943	0.201e−1	0.2949000	0.206	246.237	7.34e−4
27.598	0.212e−1	0.3016000	0.199	467.418	8.63e−4

Table 4: Results of our numerical computations for an almost uniformly rotating sequence of equilibrium configurations obtained fixing $b=0.383$ and $a=1.34$. This sequence will have a concave hamburger structure and it will not reach an instability although 101 configurations are computed.

$\frac{\tilde{\zeta}_{eq}}{\tilde{\zeta}_{pol}}$	j^2	$\frac{T}{\|W\|}$	$\frac{U}{\|W\|}$	$\widetilde{M}$	V.T.
1.000	0.000000	0.000000	0.500	2.710	9.55e−4
2.079	0.698e−2	0.1620000	0.338	5.299	5.23e−4
3.733	0.128e−1	0.2527000	0.248	16.536	7.49e−4
6.705	0.162e−1	0.2714000	0.229	54.776	7.77e−4
12.041	0.182e−1	0.2813000	0.219	150.250	1.083e−3
21.623	0.193e−1	0.2884000	0.212	378.059	9.17e−4
38.833	0.201e−1	0.2936000	0.207	915.252	6.78e−4
69.739	0.207e−1	0.2977000	0.207	2165.079	7.81e−4

which are reported in the following Tables 5, 6 and 7. Precisely the definition of quantities reported in each table is the same given in Table 1, with the exception of j^2, the squared dimensionless angular momentum, which in paper [21] is defined as

$$j^2=\frac{\widetilde{J}^2}{(4\pi)^{\frac{4}{3}}\widetilde{M}^{\frac{10}{3}}\sigma_{max}^{\frac{n}{3}}}, \tag{3.2}$$

where dimensionless quantities are again defined in Table 1 and σ_{max} is the maximum value of the dimensionless density of configuration. It is worth noting that with rotation law given in Eq. (2.17), keeping parameter $B=0$, one obtains exactly the same aforementioned j-const rotation law. We will now turn to compare results of our computations with values given in Tables 5, 6 and 7, plotting each quantity as a function of axis ratio in the subsequent figures. Calculations have been performed using several numerical grids,

https://doi.org/10.4208/cicp.OA-2017-0007 Published online by Cambridge University Press

Table 5: Results for numerical computations taken from [21] $A=2.0r_s$.

$\frac{\zeta_{eq}}{\zeta_{pol}}$	j^2	$\frac{T}{\lvert W\rvert}$	$\frac{U}{\lvert W\rvert}$	V.T.
1.050	2.966e−4	9.183e−3	0.4911	5.7e−4
1.276	1.622e−3	4.530e−2	0.4549	4.8e−4
1.551	3.0228e−3	7.689e−2	0.4233	4.1e−4
1.886	4.244e−3	9.991e−2	0.4003	4.3e−4
2.292	4.766e−3	1.086e−1	0.3916	4.3e−4

Table 6: Results for numerical computations taken from [21] $A=0.2r_s$.

$\frac{\zeta_{eq}}{\zeta_{pol}}$	j^2	$\frac{T}{\lvert W\rvert}$	$\frac{U}{\lvert W\rvert}$	V.T.
1.050	1.521e−4	7.236e−3	0.4931	5.7e−4
1.340	9.305e−4	4.323e−2	0.4570	5.3e−4
1.710	1.789e−3	7.514e−2	0.4251	4.9e−4
2.183	2.616e−3	1.022e−1	0.3991	5.0e−4
2.786	3.446e−3	1.220e−1	0.3783	5.1e−4
3.386	4.089e−3	1.356e−1	0.3647	5.0e−4
4.538	5.037e−3	1.528e−1	0.3475	4.6e−4
5.792	5.840e−3	1.651e−1	0.3352	4.6e−4
7.392	6.639e−3	1.762e−1	0.3240	4.7e−4
9.434	7.446e−3	1.864e−1	0.3138	4.8e−4
12.04	8.290e−3	1.961e−1	0.3042	4.6e−4

Table 7: Results for numerical computations taken from [21] $A=0.02r_s$.

$\frac{\zeta_{eq}}{\zeta_{pol}}$	j^2	$\frac{T}{\lvert W\rvert}$	$\frac{U}{\lvert W\rvert}$	V.T.
1.050	3.393e−6	4.472e−4	0.4998	5.8e−4
1.710	5.310e−5	6.282e−3	0.4940	5.6e−4
2.786	1.253e−4	1.302e−2	0.4872	5.5e−4
3.920	1.896e−4	1.808e−2	0.4822	5.5e−4
6.385	3.098e−4	2.596e−2	0.4743	5.5e−4
9.434	4.392e−4	3.331e−2	0.4670	5.5e−4
14.64	6.332e−4	4.305e−2	0.4572	5.4e−4
25.03	9.597e−4	5.705e−2	0.4432	5.4e−4
38.83	1.315e−3	6.996e−2	0.4303	5.2e−4
60.24	1.771e−3	8.428e−2	0.4160	5.1e−4
89.01	2.277e−3	9.806e−2	0.4022	5.0e−4

https://doi.org/10.4208/cicp.OA-2017-0007 Published online by Cambridge University Press

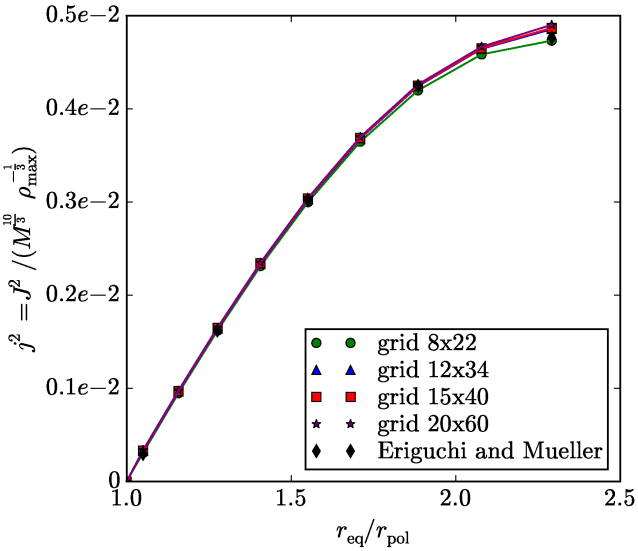


Figure 9: Comparison of results obtained with our own implementation of method by Eriguchi and Mueller and results from Table 5 (thus taking $A = 2.0r_s$), where dimensionless squared angular momentum j^2 is plotted as a function of axis ratio $\frac{r_{eq}}{r_{pol}}$.

to obtain different resolution in configurations. Namely, we considered $N_T \times N_R = 8 \times 22$ (green dots in figures), 12×34 (blue triangles), 15×40 (red squares) and 20×60 (purple stars) and in each plot results by Eriguchi and Mueller are represented by black diamonds. In addition, three different values of the rotational parameter have been considered, analogously to results presented in Tables 5, 6 and 7. The step factor for axis ratio change has been taken as 1.05 for the construction of each sequence.

From Figs. 2, 3, 9, 10, 11, 12, 13, 14, 15, 16 and 17 a grid dependent behavior arises from computation: in effect we could not obtain the entire sequences of configurations for all grids considered. For example, if one takes a grid of 10×30 points, the code reaches an error in the Newton-Raphson method. This instability of the code can occur due to the method's implementation. In addition, considering again a step factor "too" small for axis ratio from one configuration to the subsequent, some numerical oscillations occur, most of all in the first sequence of configurations, that is the one in which $A = 2.0r_s$ (or in other words the most rigid one). On the other hand, from these figures the reader can easily notice that deviations from results of paper [21] are negligible thus we may conclude that our code is well calibrated. Moreover, deviations between results obtained with grid 15×40 (red squares) and 20×60 (purple stars) could not be observed, thus, the suggestion given in [21] to use a 15×40 grid to obtain accurate results is confirmed.

In conclusion, it is worth to remember the softening condition taken in [33], where variables are updated from one iteration to another with a softening parameter, usually between 0.5 and 1.0, which often reduce numerical oscillations increasing the rate of convergence. Further studies in this direction would be useful in the present framework.

https://doi.org/10.4208/cicp.OA-2017-0007 Published online by Cambridge University Press

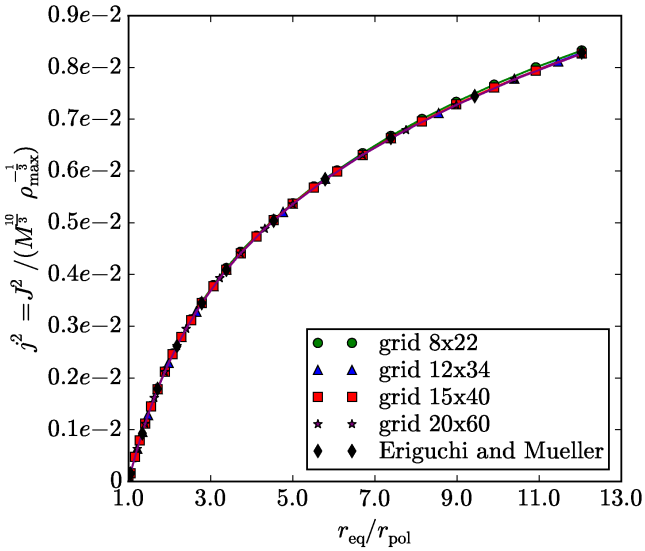


Figure 10: Same as Fig. 9 but in comparison with results from Table 6 (thus taking $A=0.2r_{\rm s}$).

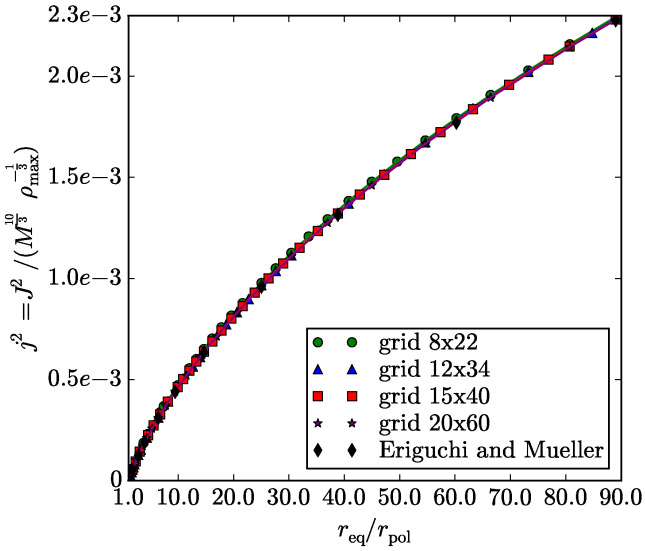


Figure 11: Same as Fig. 9 but in comparison with results from Table 7 (thus taking $A=0.02r_{\rm s}$).

4 Summary and discussion

In this paper we have implemented a multi-parametric rotation law proposed in [25] with the method introduced by Eriguchi and Mueller in [21] and studied in detail the corresponding configurations. We had treated the stability of differentially rotating polytropic stars against violations of Solberg-Høiland criterion and mass-shedding, analysing the

https://doi.org/10.4208/cicp.OA-2017-0007 Published online by Cambridge University Press

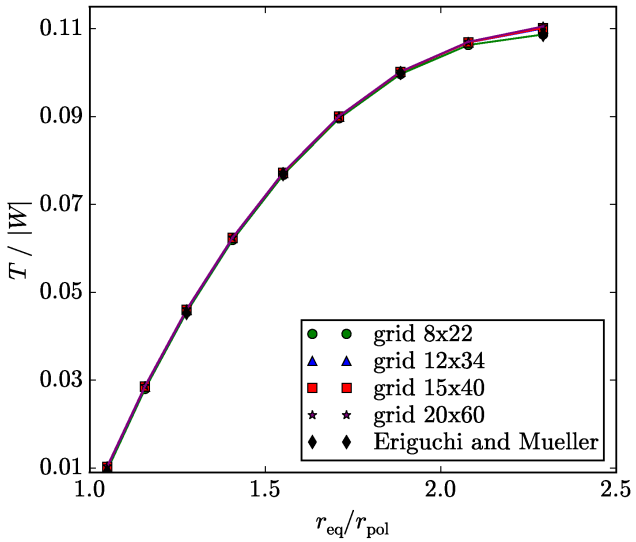


Figure 12: Comparison of results obtained with our own implementation of method by Eriguchi and Mueller and results form Table 5 (thus taking $A=2.0r_{\rm S}$), where ratio between rotational kinetic energy and gravitational potential energy is plotted as a function of axis ratio $\frac{r_{\rm eq}}{r_{\rm pol}}$.

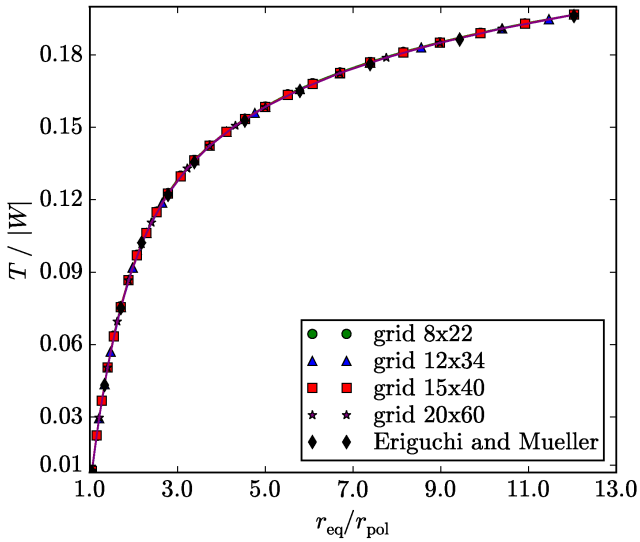


Figure 13: Same as Fig. 12 but in comparison with results from Table 6 (thus taking $A=0.2r_{\rm S}$).

free-parameters' space in search of sort of catastrophic points at which small changes in free-parameters can lead to relevant changes in the equilibrium configuration (e.g. from a concave hamburger to an ellipsoidal one) or to instabilities. It is worth noting that the rotation law as a function of the distance from the axis of rotation (namely the cylindrical

https://doi.org/10.4208/cicp.OA-2017-0007 Published online by Cambridge University Press

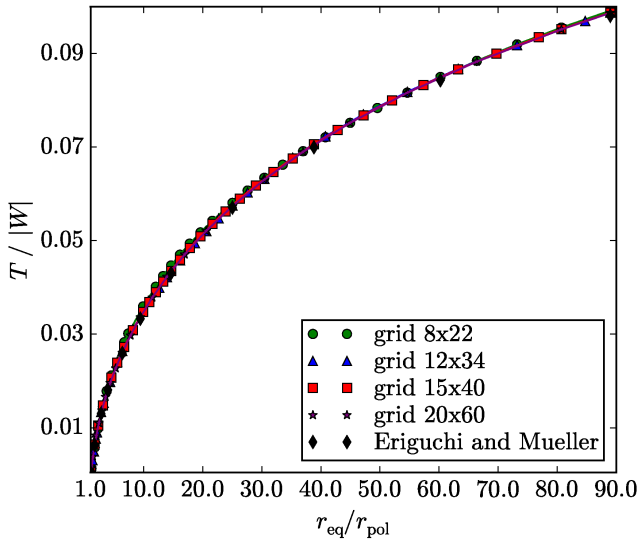


Figure 14: Same as Fig. 12 but in comparison with results from Table 7 (thus taking $A = 0.02 r_s$).

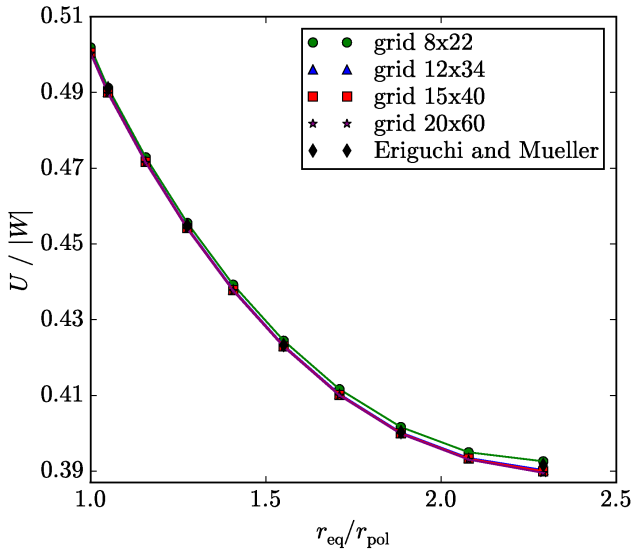


Figure 15: Comparison of results obtained with our own implementation of method by Eriguchi and Mueller and results form Table 5 (thus taking $A = 2.0 r_s$), where ratio between thermal energy and gravitational potential energy is plotted as a function of axis ratio $\frac{r_{eq}}{r_{pol}}$.

radius) introduced in Eq. (2.17) in a strictly decreasing one. For future studies, we would like to stress the necessity to focus on achievement of an improved convergence, as already mentioned in Section 3, possibly obtained by introducing a softening condition as the one presented in [33]. In addition, it would be interesting also to implement a non-

https://doi.org/10.4208/cicp.OA-2017-0007 Published online by Cambridge University Press

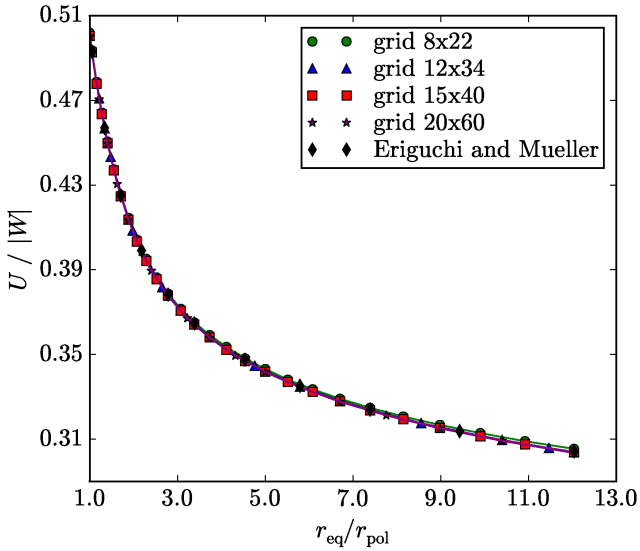


Figure 16: Same as Fig. 15 but in comparison with results from Table 6 (thus taking $A=0.2r_s$).

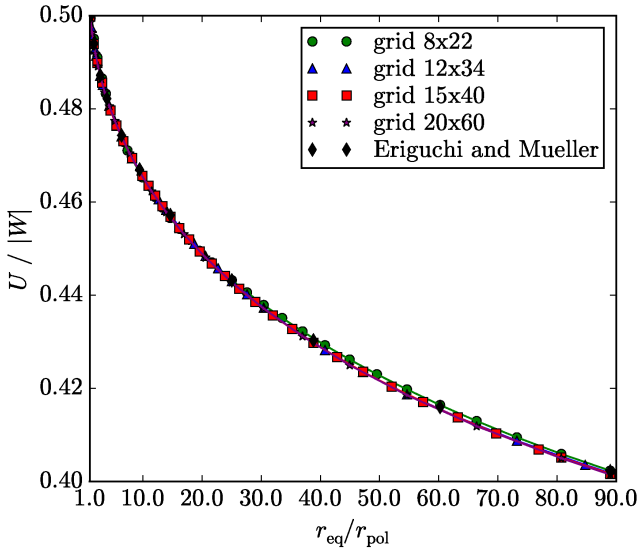


Figure 17: Same as Fig. 15 but in comparison with results from Table 7 (thus taking $A=0.02r_s$).

completely decreasing rotation law, where angular velocity may also increase in small portion of the configuration, e.g. one interesting case could be, for instance, the one in which the angular velocity in not a strictly decreasing function of the cylindrical radius as in the case of the coalescence of the two component of a binary system (for example of white dwarfs), during merging. In effect the idea to perform numerical integration in order to obtain the centrifugal potential allows one to study every kind of rotation law, and

https://doi.org/10.4208/cicp.OA-2017-0007 Published online by Cambridge University Press

studying the free-parameters space as in the way we propose, should in general allow to locate instability points. We would also focus the attention to the fact that the method presented in [21] is in principle a general one, thus it should allow to consider different kinds of EOS. In the present case, all previously presented results were obtained with a $n=1.5$ polytropic EOS, but it could also be interesting to treat the case of a numerical EOS, in which no analytical relation is known.

Appendix

A Numerical implementation and physical properties

A.1 Numerical method

Once an EOS and a rotation law are supplied, to solve the system of equations defined by Eqs. (2.14), (2.15) and (2.12), in [21] a numerical method has been presented in which the interior of the star is discretized in a mesh of points. Considering spherical coordinates, a grid is built dividing the domain into N_T points along the θ-direction, and in N_R points along each r-direction. Grid points are defined as follows:

$$\theta_i = \frac{\pi}{2}\frac{i-1}{N_T-1}, \quad i=1,\cdots,N_T, \tag{A.1}$$

$$r_{ij} = r_j(\theta_i) = r_{\text{surf}}(\theta_i)\frac{j}{N_R}, \quad i=1,\cdots,N_T, \ \ j=1,\cdots,N_R. \tag{A.2}$$

In particular, this grid does not consider the center of configuration because it has to be treated separately from other points. Note in addition that the angular values vary between 0 and $\frac{\pi}{2}$, as equatorial symmetry is taken into account, while there is no dependence on the φ coordinate as expected by axial symmetry. Then, with the use of dimensionless variables as given in Table 1 it is possible to discretize the equations. Explicitly writing the system for the fixed EOS and the rotation law, one can note that a model is completely determined by the prescription of polytropic constant K, central density ρ_c and angular velocity Ω (this last condition holds in the case of uniform rotation; in case of differential rotation one should instead fix the central value of angular velocity only, knowing that the values in all other points are given by the chosen rotation law). In the method by Eriguchi and Mueller [21], it is stressed that fixing the angular velocity is not the best way to solve the system of equation. Instead a better choice for numerical calculation is to fix the axis ratio, namely $\frac{r_{\text{eq}}}{r_{\text{pol}}} = \frac{r_{N_R}(\frac{\pi}{2})}{r_{N_R}(0)} = \frac{\tilde{\varsigma}_{\text{eq}}}{\tilde{\varsigma}_{\text{pol}}}$, the last equality obtained by the introduction of the dimensionless radial coordinate. This condition gives one last equation which will make the system solvable (see discussion on the number of equations and variables at the end of the present section). Now we can write the discretized system of equations, which will read as follows:

https://doi.org/10.4208/cicp.OA-2017-0007 Published online by Cambridge University Press

(i) at the centre of configuration:

$$1+\Psi_{\text{centre}}=C, \tag{A.3}$$

$$\Psi_{\text{centre}}=-\sum_{p=1}^{N_T}\sin(\theta_p)\Theta_p\sum_{q=1}^{N_R}\xi_{pq}R_{pq}\sigma_{pq}^n; \tag{A.4}$$

(ii) at all the grid points:

$$\sigma_{ij}+\Psi_{ij}-\frac{1}{2}\nu\xi_{ij}^2\sin(\theta_i)^2=C, \tag{A.5}$$

$$\Psi_{ij}=-\sum_{p=1}^{N_T}\sin(\theta_p)\Theta_p\sum_{q=1}^{N_R}\xi_{pq}^2R_{pq}\sigma_{pq}^n \cdot\sum_{m=0}^{\infty}f_{2m}(\xi_{ij},\xi_{pq})P_{2n}(\cos(\theta_i))P_{2n}(\cos(\theta_p))\sigma_{pq}^n; \tag{A.6}$$

(iii) boundary conditions to define the surface:

$$\sigma_{i,N_R}=0, \quad \text{for } i=1,\cdots,N_T; \tag{A.7}$$

(iv) a last equation for the axis ratio:

$$\frac{\xi_{N_T,N_R}}{\xi_{1,N_R}}=\lambda. \tag{A.8}$$

To note that in Eqs. (A.4) and (A.6), the integral over the volume is discretized. In particular, the terms Θ_p and R_{pq} denote respectively angular and radial grid spacings multiplied by weight factors which depend on the numerical integration scheme which in radial direction is the Simpson rule while in angular direction is the trapezoidal rule. The system of $N_T\times(N_R+1)+2$ equations for the same number of unknowns (namely N_T surface radii, $N_T\times N_R$ densities in each grid-point, the central value of angular velocity and the integration constant which turns out to be the gravitational potential at the pole) can be solved using an iterative numerical method, such the one called the Newton-Raphson's. The Newton-Raphson's method in [21] starts from a spherical (non-rotating) configuration and gradually increases the axis ratio of the configuration by a constant factor near 1 (for example 1.05 or less) to obtain a new configuration and then repeats the procedure until a certain stopping condition is reached. The computation of a spherically symmetric model (meant as the density distribution and the surface radius) of a polytropic star of index n is a well-known problem in astrophysics and it was studied by many authors in the past (see e.g. [30]). The equation to solve, namely the Lane-Emden equation, reads

$$\frac{1}{\xi^2}\frac{\partial}{\partial\xi}\left(\xi^2\frac{\partial\sigma(\xi)}{\partial\xi}\right)+\sigma(\xi)^n=0, \tag{A.9}$$

https://doi.org/10.4208/cicp.OA-2017-0007 Published online by Cambridge University Press

where we have adopted the same notation for dimensionless variables as in the Section 1. One can solve Eq. (A.9) numerically, finding $\sigma(\xi)$, imposing as initial conditions

$$\sigma(0)=1, \tag{A.10a}$$

$$\sigma'(0)=0. \tag{A.10b}$$

Through a Newton-Raphson iteration scheme, one can also find the zero of function $\sigma(\xi)$, which represents the surface radius of the spherical solution. Finally, one can put $\nu=\nu_0=0$ and find $C\equiv C_0$ with expression given by Eq. (A.5) in which Eq. (A.6) can be used.

A.2 Definition of relevant physical quantities

Once the density distribution and surface radii of a configuration are computed, one could also evaluate its physical properties (cf. [27] and [31]). Firstly, the rotational kinetic energy of a rotating configuration can be found with the following expression

$$T=\frac{1}{2}\int_V \rho\varpi^2\Omega^2 dV, \tag{A.11}$$

where V is the volume, ϖ is the cylindrical radius (distance from the axis of rotation, thus $\varpi=r\sin(\theta)$ when spherical coordinates are considered) and ρ represents as usual the density. The gravitational potential energy, on the other hand, can be computed as

$$W=-\frac{1}{2}G\int_V \rho\Phi_g dV, \tag{A.12}$$

being G the constant of gravitation and Φ_g the gravitational potential, which can be computed with Eq. (2.11). The internal energy of the system reads as

$$U=\frac{1}{\gamma-1}\int_V \rho dV, \tag{A.13}$$

where γ is the polytropic adiabatic exponent defined as $\gamma=1+\frac{1}{n}$. Obviously the total mass of the configuration is simply

$$M=\int_V \rho dV, \tag{A.14}$$

while the total angular momentum is given by

$$J=\int_V \rho\Omega\varpi^2 dV. \tag{A.15}$$

Finally another quantity which is worth computing is the value of virial test, which in [21] (just as in [32]) is expressed in the following form

$$V.T.=\left|\frac{(2T+W+3(\gamma-1)U)}{W}\right|, \tag{A.16}$$

and it should be zero in order to have an accurate model.

https://doi.org/10.4208/cicp.OA-2017-0007 Published online by Cambridge University Press

Acknowledgments

C.C. and S.F. acknowledge INdAM-GNFM and ICRANet for support. J.A.R. acknowledges partial support of the project No. 3101/GF4 IPC-11/2015 and the target program of the Ministry of Education and Science of the Republic of Kazakhstan.

References

[1] Chandrasekhar, S., 1967: An Introduction to the Study of Stellar Structure, Dover.
[2] Chandrasekhar, S., 1987: Ellipsoidal Figures of Equilibrium, Dover.
[3] James R. A., 1964: The Structure and Stability of Rotating Gas Masses, Astrophys. J., 140, 552-582.
[4] Busarello, G., Filippi, S. and Ruffini R., 1988: Anisotropic tensor virial models for elliptical galaxies with rotation or vorticity, Astron. Astrophys., 197, 91-104.
[5] Busarello G., Filippi S. and Ruffini R., 1989: Anisotropic and inhomogeneous tensor virial models for elliptical galaxies with figure rotation and internal streaming, Astron. Astrophys., 213, 80-88.
[6] Busarello G., Filippi S. and Ruffini R., 1990: 'b-type' spheroids, Astron. Astrophys., 227, 30-32.
[7] Filippi S., Ruffini R. and Sepulveda A., 1990: Generalized Riemann configurations and Dedekind's theorem - The case of non-linear internal velocities, Astron. Astrophys., 231, 30-40.
[8] Filippi, S.; Ruffini, R.; Sepulveda, A. 1990: On the generalization of Dedekind-Riemann sequences to nonlinear velocities., Europhys. Lett., 12, 735-740.
[9] Filippi, S.; Ruffini, R.; Sepulveda, A., 1990: Nonlinear velocities in generalized Riemann ellipsoids., Nuovo Cim. B, 105, 1047-1054.
[10] Filippi S., Ruffini R. and Sepulveda A., 1991: Generalized Riemann ellipsoids - Equilibrium and stability, Astron. Astrophys., 246, 59-70.
[11] Filippi S., Ruffini R. and Sepulveda A., 1996: On the Implications of the nth-Order Virial Equations for Heterogeneous and Concentric Jacobi, Dedekind, and Riemann Ellipsoids, Astrophys. J., 460, 762
[12] Filippi S., Ruffini R. and Sepulveda A., 2002: Functional approach to the problem of self-gravitating systems: Conditions of integrability, Phys. Rev. D, 65, 044019.
[13] Eriguchi Y. and Sugimoto D. 1981: Another Equilibrium Sequences of Self-Gravitating and Rotating Incompressible Fluid, Prog. Theor. Phys., 65, 1870-1875.
[14] Sugimoto D., Nomoto K. and Eriguchi Y. 1981: Stable Numerical Method in Computing of Stellar Evolution, Prog. Theor. Phys. Supp., 70, 115-131.
[15] Eriguchi Y. and Hachisu I., 1982: New Equilibrium Sequences Bifurcating from Maclaurin Sequence, Prog. Theor. Phys., 67, 844-851.
[16] Eriguchi Y., Hachisu I. and Sugimoto D., 1982: Dumb-Bell Shape Equilibrium and Mass Shedding Pear-Shape of Self-Gravitating Incompressible Fluid, Prog. Theor. Phys., 67, 1068-1075.
[17] Hachisu I., Eriguchi Y., and Sugimoto D. 1982: Rapidly Rotating Polytropes and Concave Hamburger Equilibrium, Prog. Theor. Phys., 68, 191-205.
[18] Hachisu I. and Eriguchi Y., 1982: Bifurcation and Fission of Three Dimensional, Rigidly Rotating and Self-Gravitating Polytropes, Prog. Theor. Phys., 68, 206-221.

https://doi.org/10.4208/cicp.OA-2017-0007 Published online by Cambridge University Press

[19] Eriguchi Y. and Hachisu I., 1983: Two Kinds of Axially Symmetric Equilibrium Sequences of Self-Gravitating and Rotating Incompressible Fluid, Prog. Theor. Phys., 69, 1131-1136.
[20] Hachisu I. and Eriguchi Y., 1983: Bifurcation and Phase Transitions of Self-Gravitating and Uniformly Rotating Fluid, Mon. Not. R. Astron. Soc., 204, 583-589.
[21] Eriguchi Y. and & Mueller E.: 1985, A general computational method for obtaining equilibria of self-gravitating and rotating gases, Astron. Astrophys., 146, 260-268.
[22] Stoeckly R., 1965: Polytropic Models with Fast, Non-Uniform Rotation, Astrophys. J., 142, 208-228.
[23] Fujisawa K., 2015: A versatile numerical method for obtaining structures of rapidly rotating baroclinic stars: self-consistent and systematic solutions with shellular-type rotation, Mon. Not. R. Astron. Soc., 454, 3060-3072.
[24] Galeazzi F., Yoshida S. and Eriguchi Y., 2012: Differentially-rotating neutron star models with a parametrized rotation profile, Astron. Astrophys., 541, A156.
[25] Cherubini C., Filippi S., Ruffini R., Sepulveda A. and Zuluaga J. I., 2008: Non-Homogeneous Axisymmetric Models of Self-Gravitating Systems. The Eleventh Marcel Grossmann Meeting On Recent Developments in Theoretical and Experimental General Relativity, Gravitation and Relativistic Field Theories, 2340-2342.
[26] Tassoul, J.-L., 1978: Theory of rotating stars. Princeton Series in Astrophysics, Princeton University Press.
[27] Horedt, G. P., 2004: Polytropes - Applications in Astrophysics and Related Fields. Kluwer Academic Publishers.
[28] Maeder, A., 2009: Physics, Formation and Evolution of Rotating Stars. Astronomy and Astrophysics, Springer, Berlin.
[29] Press, W. H., Teukolsky, S. A., Vetterling, W. T. and Flannery, B. P., 1992: Numerical recipes in C. The art of scientific computing. Cambridge University Press, 2nd ed.
[30] Chandrasekhar S., 1933: The equilibrium of distorted polytropes. I. The rotational problem, Mon. Not. R. Astron. Soc., 93, 390-406.
[31] Chandrasekhar S., 1961: Hydrodynamic and hydromagnetic stability. Dover Publications.
[32] Ostriker J. P. and Bodenheimer P., 1968: Rapidly Rotating Stars. II. Massive White Dwarfs, Astrophys. J., 151, 1089-1098.
[33] Uryū K., Limousin F., Friedman J.L., Gourgoulhon E. and Shibata, M., 2009: Nonconformally flat initial data for binary compact objects, Phys. Rev. D, 80, 124004.

https://doi.org/10.4208/cicp.OA-2017-0007 Published online by Cambridge University Press